

3 Sub-Micron Structuring of LiNbO₃ Crystals with Multi-Period and Complex Geometries

S. Grilli and P. Ferraro

3.1 Introduction

Lithium niobate (LN) is a ferroelectric material which has attracted a considerable interest in different fields, such as the optical and the laser and communications industry, due to its excellent nonlinear optical, electro-optic, piezoelectric and acousto-optical coefficients [1]. LN is widely used in the laser area, where fabrication of periodically poled materials has achieved high efficiencies in quasi-phased matched nonlinear interactions [2], but also in the field of microwave communications for surface acoustic wave delay lines [3]. Recently, the possibility to microstructure LN crystals has been attracted great interest for the useful applications foreseen in the fields of optics and optoelectronics. However, those applications require anisotropic etching techniques and different methods have been reported for machining and microstructuring in LN, as described in Sect. 3.2. Section 3.3 describes the electric field overpoling technique as a useful tool for sub-micron structuring by subsequent differential wet etching, while Sect. 3.4 describes the holographic lithography (HL) process used for submicron periodic poling. Sections 3.5 and 3.6 present the wide variety of surface structures obtained by overpoling and etching. Conclusions and discussion are summarized in Sect. 3.7.

3.2 Overview of the Etching Techniques Applied to Lithium Niobate

The desirability of etching LN to form surface structures is widely recognized and different techniques have been tried on this material in the past, such as mechanical grinding [4], ion milling [5], sputter etching [6], plasma etching [7]. None of these methods provided entirely satisfactory results. In fact, mechanical grinding can produce only rather large structures with a limited range of geometries, while ion milling and sputter etching can result in substrate faceting and redeposition of sputtered material on the substrate. Furthermore, these etching techniques do not differentiate strongly between substrate and mask so that poor etching selectivity is provided. Among those the plasma etching, which is basically a dry-chemical etch

process, was the only technique able to give high selectivity but its first applications to LN substrates produced very slow etch rates [7]. The wet etching is widely used in the field of material processing but is rarely applied to LN because of the well known material's strong etch resistance which results in low etch rates and sometimes non-uniform etching. On the other hand the wet etching of LN has been typically used to reveal domain polarity and defect topology [8–10] by immersion in a HF/HNO_3 acid mixture. In fact, this mixture exhibits the property to etch the negative Z face of the crystal while the positive is left essentially untouched. Nevertheless great effort has been spent during the last decade in order to improve the reliability of the wet etching in case of LN material. The introduction of structural defects accelerates the etching rate so that the combination of a defectiveness agent, such as ion bombardment or laser ablation, with subsequent wet etching has been demonstrated to be a useful method for etching of LN.

In this section a brief overview is given of the most important techniques, presented in literature during the last years, in order to get reliable microstructuring of LN crystal substrates. These include reactive ion etching (RIE) [11, 12], laser ablation below and over the band-gap of the material [13, 14], wet etching of proton exchanged material [15–17], wet etching of periodically poled crystals [18], electron beam bombardment [19], laser frustrated wet etching [20], ion implantation [21], focused ion beam bombardment [22], and more recently plasma etching of proton-exchanged samples [23], improved wet etching [24]. Another technique was proposed by the authors in [25] where periodic structures at sub-micron scale were fabricated by wet etching samples after specific ferroelectric domain manipulation.

The RIE presented in [11, 12] was a method combining some advantages of both plasma and sputter etching. The etching agent was represented by a low-pressure plasma of chemically active gases formed in a parallel plate radiofrequency sputtering station. The combination of a long mean free path and an electric field at the sample yielded anisotropic etching, thus minimizing the undercut and leading to high resolution. Ideally the reaction creates volatile products so that, unlike the case for sputter etching, the redeposition was strongly reduced. The laser ablation technique was presented in literature under different operating conditions. The method in [13] involved spatially localized melting of LN by high power density laser pulses with photon energies in excess of the band-gap of LN. Powdered or small crystals of KF were applied directly to the surface prior to irradiate the substrates with laser pulses. While molten, LN undergoes reaction with KF to form complex niobium oxyfluoride anions by fusion of salts. The resulting solid was highly water soluble so that the insolubility of LN permitted subsequent removal of only the irradiated area by rinsing in water. The technique presented in [14] made use of a laser irradiation process below the band-gap of LN by using a cw Argon laser emitting at 351 nm with a maximum power of 2.5 W. The process was basically a reduction process utilizing photon energies of about 3.5 eV, thus enabling selective removal of the laser-processed substrate by subsequent wet etching of the Y-cut LN substrates. The possibility to fabricate groove-like structures for precise fibre positioning was demonstrated and Fig. 3.1 shows the corresponding SEM images.

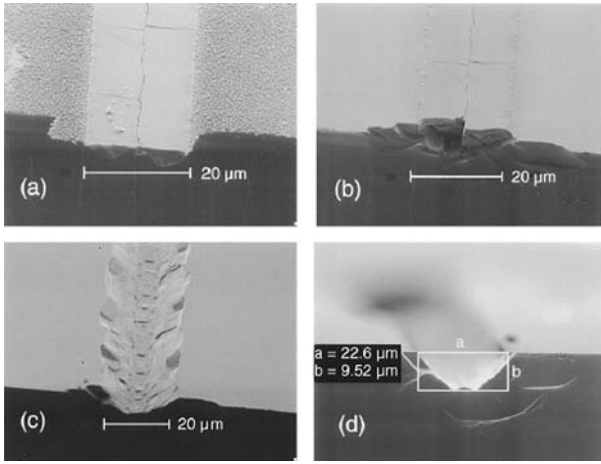


Fig. 3.1. LN sample after laser processing. (a) Before any cleaning; (b) after cleaning with ethanol; (c), (d) and after hot HF etch (from [14])

The wet etching process proposed in [15] consisted in selective etching of proton exchanged regions by using a mixture of HF and HNO₃. Since the first experiments in [26], proton exchange (PE) and annealed proton exchange (APE), by using benzoic acid as the proton source, are still widely used techniques to fabricate waveguides of relatively good quality in LN [27] and the results in [15] show the possibility to use this technique for selective surface etching of LN samples by a relatively simple process, consisting basically in the immersion of the LN sample in an acid, often a benzoic acid melt, at around 200°C for minutes up to hours.

LN has two stable domain orientations and microstructuring through domain manipulation followed by differential etching was developed in [18]. The process consisted in domain patterning by electric field poling followed by etching in a mixture of HF and HNO₃. A variety of structures at micron and sub-micron scale was produced by this technique and the surface quality of the structures was relatively smooth and straight as shown in Fig. 3.2.

The same group proposed later a laser frustrated etching process as an advanced technique for the fabrication of self-ordered sub-micron structures in iron-doped LN substrates [20], and Fig. 3.3 shows a SEM image of the fabricated structures as example.

One- and two-dimensional structures at sub-micron scale were fabricated by electron beam bombardment associated to chemical etching as presented in [19]. The electron beam was used to reverse the ferroelectric domains locally and subsequent etching revealed the surface structure. Figure 3.4 shows the SEM image of a two-dimensional structure obtained by this technique.

In [21] the possibility to fabricate high-quality ridge waveguides in Z-cut LN by oxygen ion implantation associated to wet etching was proposed. The technique allowed to obtain ridge structures up to 3.5 μm deep and thus suitable for ridged

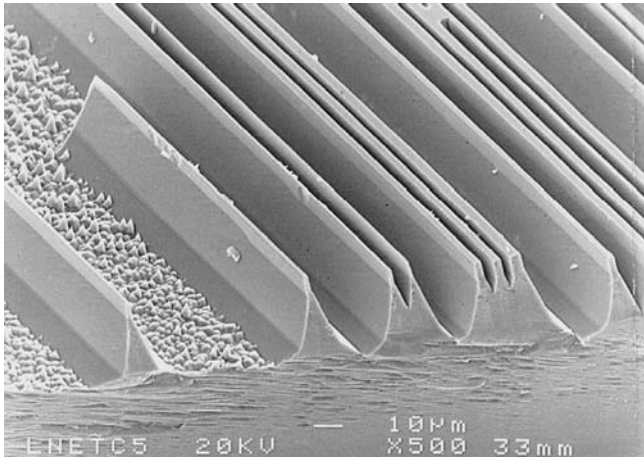


Fig. 3.2. SEM image of the structures obtained by domain manipulation and subsequent etching (from [18])

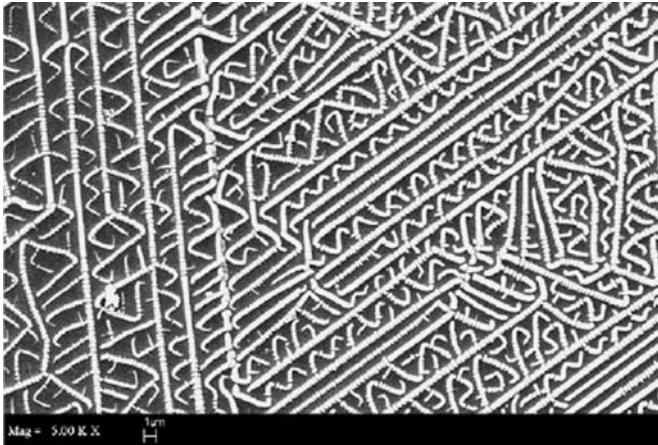


Fig. 3.3. SEM image of self-ordered structures, as example (from [20])

modulator applications. Figure 3.5 shows the cross sectional profile of the ridge waveguide fabricated by this technique.

Recently, the focused ion-beam bombardment was proposed as an alternative technique for surface etching of LN substrates [22]. Photonic band gap structures with a spatial resolution of 70 nm were obtained. The method provided high resolution and the ability to drill holes directly from the sample surface. The only constraint was that the sample surface had to be metallized and grounded to avoid charge accumulation. Figure 3.6 shows the focused-ion-beam image of the cross-section of the fabricated cavities. The array exhibited well defined circular holes with etching depth of approximately 2 μm .

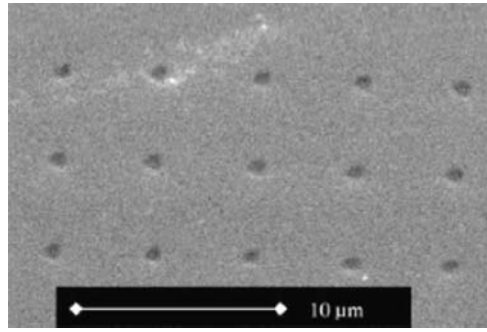


Fig. 3.4. SEM image of a two-dimensional structure obtained by electron beam bombardment and subsequent etching (from [19])

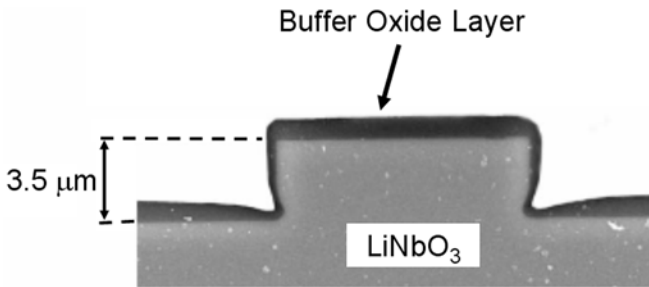


Fig. 3.5. Cross sectional profile of the ridge waveguide (from [21])

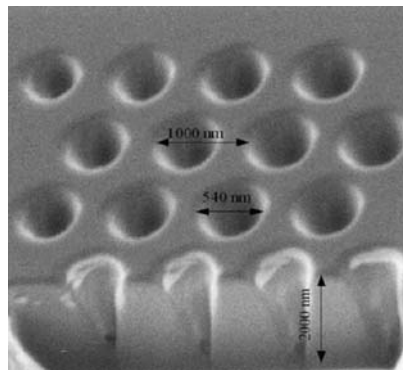


Fig. 3.6. Focused-ion-beam image of the fabricated structures (from [22])

The plasma etching of LN substrates was proposed very recently [23]. The novelty of the technique was based on the use of fluorine gases on proton-exchanged substrates in order to prevent redeposition of LiF and thus enabling the fabrication of deeper structures. Figure 3.7 shows the SEM image of the end face of the ridge structure obtained by this technique.

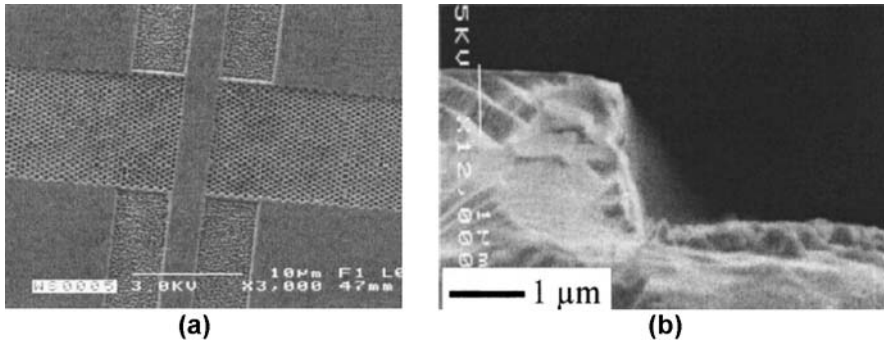


Fig. 3.7. (a) SEM image of the photonic crystal waveguide with a periodic structure at 500 nm distance between holes; (b) SEM image of the end face of the ridge structure (from [23])

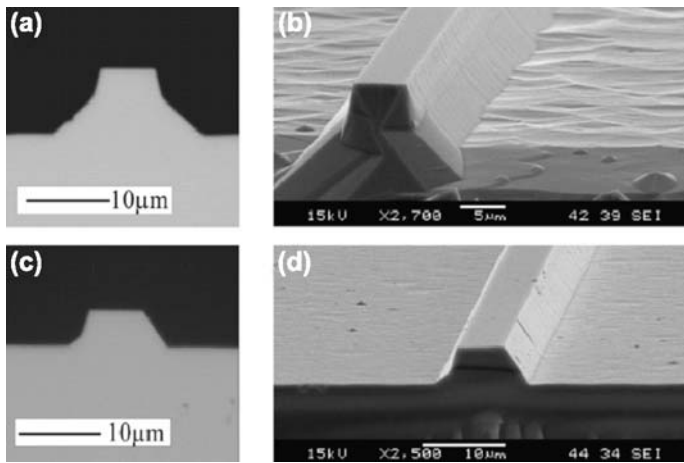


Fig. 3.8. (a) optical microscope image of the end face of a Y propagating ridge waveguide; (b) corresponding SEM image; (c) optical microscope image of the end face of a X propagating ridge structure; (d) corresponding SEM image (from [24])

The wet etching process is in continuous evolution and very recently new encouraging results were presented in case of LN substrates [24]. Ridge waveguides were fabricated by a mixture of HF and HNO₃ acids by using chromium stripes as masks. The results showed that smooth etched surfaces were obtained by adding some ethanol into the etching solution. The structures were also tested as low-loss mono-mode waveguides with height up to 8 μm and width from 4.5 to 7.0 μm. Figure 3.8 shows the optical microscope images and the corresponding SEM images of a couple of structures obtained by this technique.

Another surface structuring technique to be mentioned was proposed recently by the authors [25]. The method is based on the periodic domain reversal by electric field overpoling and subsequent wet etching in HF solution. The overpoling process

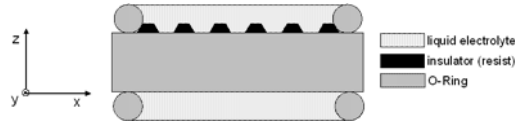


Fig. 3.9. Schematic view of the sample cross section after lithographic patterning

allowed the fabrication of sub-micron periodic structures while the conventional wet etching was used to replicate the domain pattern onto the Z cut LN crystal sample as a surface structure. The technique is relatively simple and the selective domain inversion at sub-micron scale is obtained by using fine pitch resist patterns realized by HL, as described in the following sections.

3.3 Electric Field Poling and Overpoling

Starting from a single-domain crystal, periodic domain structures can be achieved by applying external electric fields at room temperature [2, 28]. The challenge of fabricating high quality quasi-phase-matching structures by electric field poling (EFP) lies in achieving few micrometers wide domains in crystals of several millimetres in thickness. This put high demands on the poling process. Most of the last papers on periodically poled LN (PPLN), obtained by EFP, report interaction lengths of few centimeters in commercial samples of 0.5 mm thickness. Thicker samples cannot be used because of the dielectric breakdown appearing before domain inversion. Recently it has been reported the decrease of the ferroelectric coercive field by one order of magnitude between congruent and stoichiometric crystals. This makes possible the electric field fabrication of periodic structures at room temperature in few millimetres thick samples [29].

The periodic EFP (PEFP) consists of using lithographic techniques to produce a photoresist grating of the desired period to be used as a mask for applying the external electric field with a liquid electrolyte [28]. A positive voltage pulse slightly exceeding the coercive field of the material (around 21 kV/mm in LN and 2 kV/mm in KTP) is applied to the patterned crystal face by using a liquid electrolyte. The liquid electrode configuration has two electrolyte containing chambers which squeeze the sample between two O-ring gaskets, as shown schematically in Fig. 3.9.

Figure 3.10 illustrates the schematic view of the typical external electrical circuit. A conventional Signal Generator (SG) drives an High Voltage Amplifier (HVA-2000x) with a series current limiting resistor R_s in order to get a 12 kV positive voltage. A diode rectifier D is connected to the output of the HVA to prevent flowing of backswitch current in the circuit.

In case of LN the reversed domains typically grow beyond the width of the electrodes as result of the remaining fringing fields along the edges of the lithographic grating strips [28]. For example, in PPLN processed for infrared applications (periods $>10 \mu\text{m}$), the inverted domain width will typically be $\sim 3\text{--}4 \mu\text{m}$ wider than that of the electrode. To obtain the desired domain size, insulating strips wider than

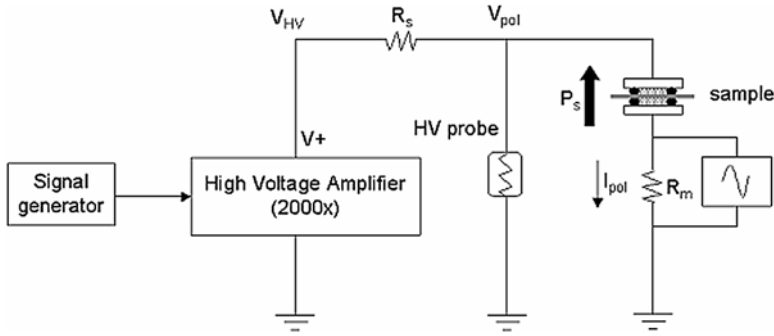


Fig. 3.10. Schematic view of the external circuit for EFP. SG signal generator; HVA high voltage amplifier; D diode rectifier; R_s series resistor; V_{pol} poling voltage; HVP high voltage probe; R_m monitoring resistor; OSC oscilloscope; I_{pol} poling current

the electrodes must be fabricated. The strategy for optimal domain patterning is to stop the voltage pulse before poling progresses under the photoresist layer. This is usually accomplished by delivering the *a priori* known amount of charge $Q = 2P_s A$ required for polarization reversal in the electrode regions [2]. An *in-situ* stopping criterion consisting in watching for a drop in the poling current I_{pol} and a corresponding rise in the poling voltage V_{pol} , both effects indicating that the sample has completely poled under the electrodes and that the domains are now laterally spreading under the insulating layer, is used [2, 28]. In fact, the conductivity of LN at room temperature is low enough that the poling current can be monitored readily by measuring the voltage drop across the R_m resistor (usually 10 k Ω) while a conventional High Voltage Probe (HVP) is used to measure the poling voltage V_{pol} across the sample. Both current and voltage waveforms are visualized on the oscilloscope OSC during the poling process. As mentioned previously, reversed ferroelectric domain patterns are usually inspected unambiguously by a well established technique based on selective wet etching [8]. Alternative approaches include the non-invasive domain visualization by crossed polarizers [30] and more recently the observation of domain structures by the EO effect [31].

The EFP is applied here by following a non-conventional procedure consisting in the application of additional electric field pulses slightly above the coercive field of the material till a drop to zero of the poling current is detected, thus ignoring both the total amount of charge delivered to the sample and the usual crucial stopping criterion. Figure 3.11(a), (b) show the typical waveforms of the poling voltage and of the poling current acquired in case of the first and the last electric field pulse, respectively. The technique is called “electric field overpoling” (EFO) and allows to fabricate periodic surface domain patterns at sub-micron scale, otherwise difficult to achieve by the conventional EFP described above.

The selective poling is achieved by using insulating resist gratings, as in case of conventional EFP, but obtained by the HL process, which allows to get finer pitch structures compared to mask lithography as described in the following section.

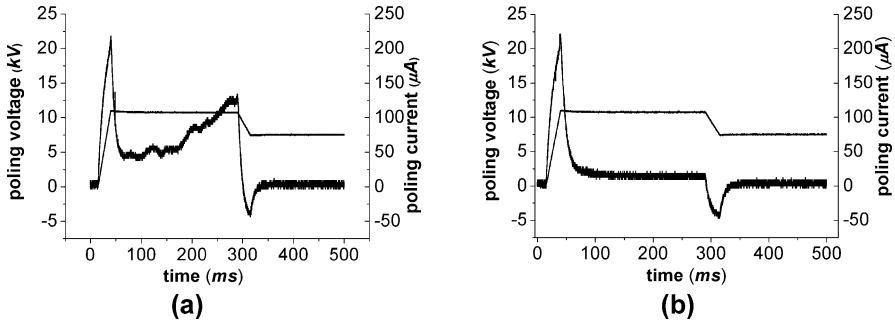


Fig. 3.11. Typical voltage and current waveforms acquired during electric field overpoling in correspondence of (a) the first and (b) the last electric field external pulse. The *thicker curve* corresponds to the current waveform while the *thinner* refers to the poling voltage

3.4 Holographic Lithography

HL is carried out by combining two coherent wavefields to form a sinusoidal intensity light pattern in space. The interferogram is generated within the volume of space defined by the overlapping beams. Since HL does not need any photolithographic mask, the field size depends only on that of the two beams, whereas in conventional mask lithography the imaging system generally limits the workable field size. A simple 1D grating can be obtained by exposing a layer of photoresist to the interference pattern. Furthermore, more complex 2D patterns, including square or hexagonal arrays of dots or holes, can be obtained by overlaying multiple exposures or combining more than two beams. HL has some unique advantages over conventional optical lithography. In particular, the spatial resolution of HL can easily exceed the resolution limits of today's optical steppers when comparable wavelengths are used. For example, structures as small as 100 nm are readily patterned by HL using a source at 351 nm [32, 33] with the additional advantage of a faster process, if compared to Electron Beam Lithography, especially when large exposed areas are required. Compared to mask optical lithography, HL is not diffraction limited and the depth of focus is effectively infinite on the scale of planar devices. This makes HL well suited for applications where substrate flatness and topography are critical issues. One more attractive feature of HL is its implementation with relatively simple optical components so that effects due to lens aberrations are dramatically reduced compared to the case of conventional lithography.

Three different set-ups have been used here to generate the interference pattern: Michelson (M); two-beams (TB); Lloyd's mirror (LM). Figure 3.12 shows the schematic views of these interferometric configurations. The period of the fringe pattern depends on the overlapping angle 2θ between the two interfering beams according to the formula $p = \lambda/2 \sin \theta$. The source used for these interferometers is a coherent He–Cd cw laser delivering a power of about 65 mW at 441.6 nm. Different fringe periods and exposed areas are provided by these interferometers, depending on the overlapping geometry of the two interfering wavefields. The M set-up pro-

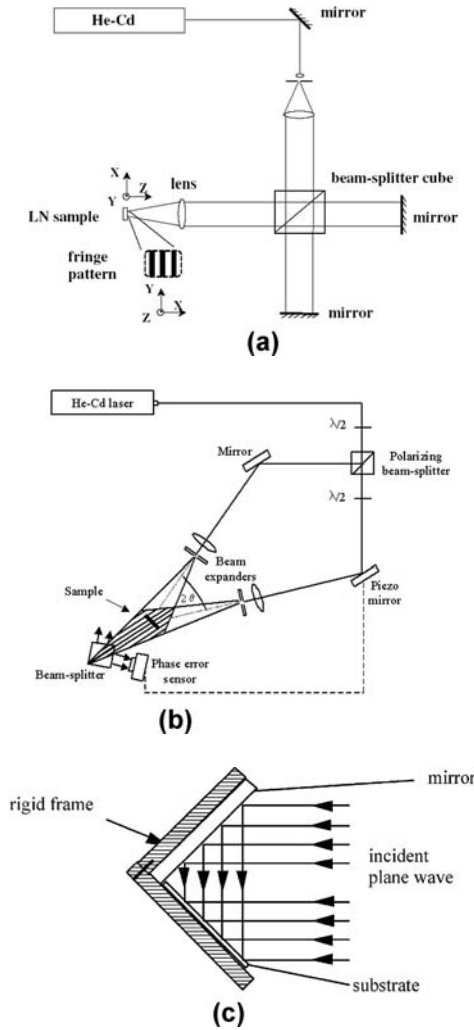


Fig. 3.12. Interferometric set-ups used for HL process: **(a)** Michelson type used for periods down to about $15\ \mu\text{m}$; **(b)** two-beams type used for periods down to the diffraction limit (about $220\ \text{nm}$) over relatively large areas (about $2\ \text{cm}$ diameter); **(c)** Lloyd's mirror type used for periods down to about $220\ \text{nm}$ over relatively small areas (about $5\ \text{mm}$ large)

vides an interferogram covering a circular region of about $25\ \text{mm}$ in diameter with a fringe period ranging from the zero fringe condition down to about $15\ \mu\text{m}$. Shorter periods are not possible due to the intrinsic limitations of the configuration which does not allow to enlarge the recombination angle of the two beams.

The TB set-up used in this work is suitable for shorter periods ranging from about $2\ \mu\text{m}$ down to about $220\ \text{nm}$ ($\lambda/2$ diffraction limit). Larger periods would be possible at narrower angles and thus at longer distances from the dividing beam-

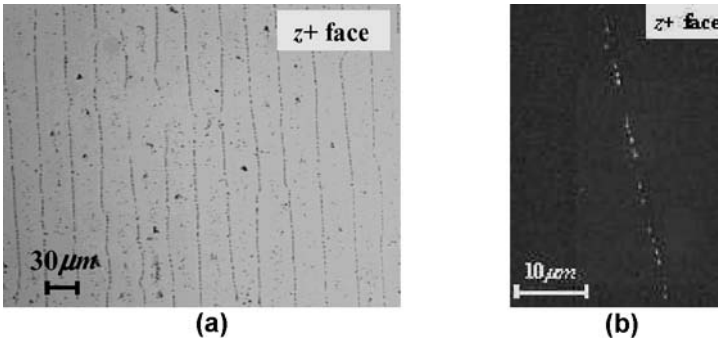


Fig. 3.13. (a) Optical microscope image of the aligned dot domains revealed by wet etching; (b) SEM image of the dot structures

splitter. The LM set-up allows to produce relatively short fringe periods like in case of the TB interferometer. In this case the coherence of the fringe gratings depends dramatically on the quality of the mirror. Dust particles on the mirror and any sharp edges give rise to scattered radiation which contributes to a coherent noise. The LM configuration is hence relatively simple and cheap, but does not produce the highest quality gratings and grids.

3.5 Periodic Sub-Micron Structuring

The EFO was applied to LN samples resist patterned with different geometries by HL as described in the following sections.

3.5.1 Overpoling Applied to One-Dimensional Michelson Resist Gratings

The EFO was applied to LN crystal samples patterned with a one-dimensional resist grating at 30 μm period obtained by the M set-up. The process was about 3 s long and the resulting ferroelectric domain pattern, revealed by a wet etching process of 60 minutes in $\text{HF}:\text{HNO}_3 = 1:2$ acid mixture, is shown in Fig. 3.13.

Aligned dot-like structures with sub-micron size are visible, corresponding to un-reversed regions under the photoresist strips. This effect is due to an incomplete merging of the adjacent reversed domains under the photoresist. The isolated dots aligned along the photoresist fringes correspond to the regions excluded by the merging of the hexagonal-type counter propagating domain walls, originating from two adjacent electrodes during poling and joining under the resist strips. The propagating domain walls are probably not straight because the sidewalls of the resist strips are affected by relatively high corrugation and low steepness. In fact, interference fringes with pitch values over the micron scale present quite large speckles such that the propagating domain walls find ways along which the velocity of motion

varies. Consequently, the merging is not successful everywhere. The optical microscope image taken in a peripheral region of the pattern and presented in Fig. 3.14 clearly supports this interpretation. It illustrates the domain merging occurring in different regions of the pattern such that the merging process is frozen in the various stages of its evolution.

The mechanism of merging of adjacent domains leads to the formation of the aligned dot-like domains under the resist strips. Microscope inspection of the etched sample reveals that opposite crystal faces exhibit different structure morphologies, as shown by the magnified optical microscope images in Fig. 3.15. A line-shape structure on Z^- face corresponds to a dot-shape on the Z^+ . One of the interesting features of these dot-like domains is the sub-micron size, as shown by the SEM image in Fig. 3.13(b). In fact, despite the advantages achieved nowadays by the conventional EFP, such as repeatability, scalability and applicability over a wide range of materials, fabrication of periodically poled materials with arbitrarily small values of period, particularly at sub-micron scales, remains an elusive goal.

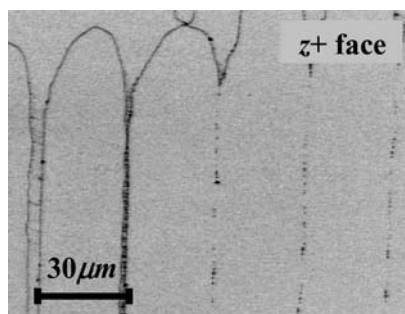


Fig. 3.14. Optical microscope image of the dot-like domains in a peripheral region of the pattern

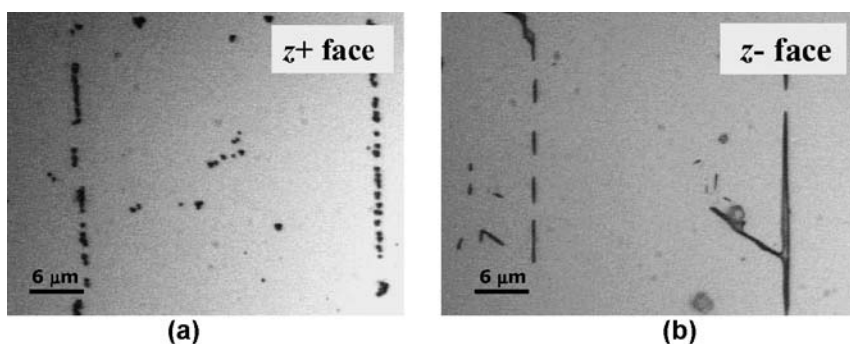


Fig. 3.15. (a) Magnified optical microscope image of the dot-like domains on Z^+ and (b) the corresponding line-like structure on Z^-

The EFO technique presented here can be considered as an effective and relatively simple solution for achieving high density and sub-micron ferroelectric reversed domain structures.

3.5.2 Overpoling Applied to Two-Dimensional Michelson Resist Gratings

The EFO technique was applied to LN crystal samples patterned with a two-dimensional resist grating obtained by two 90° crossed exposures by the M set-up. The resulting grating on Z+ face consists in a square array of photoresist dots with a period of about 23 μm along both the X and Y crystal axis direction, as shown by the optical microscope image in Fig. 3.16(a). The poling process was about 3.5 s long. Figure 3.16(b) shows the optical microscope image of the resulting square array of dot-like domains revealed by 30 minutes wet etching at room temperature. The two-dimensional geometry of the resist grating has clearly improved the period regularity of the dot-like domains along the Y crystal axis direction. In fact, these dot-like domains are equally spaced by about 20 μm along both the X and Y direction, in agreement with the pitch size of the resist grating.

As explained in the previous Section, the dot-like structures correspond to the regions left un-reversed after the domain spreading under the resist dots. The SEM

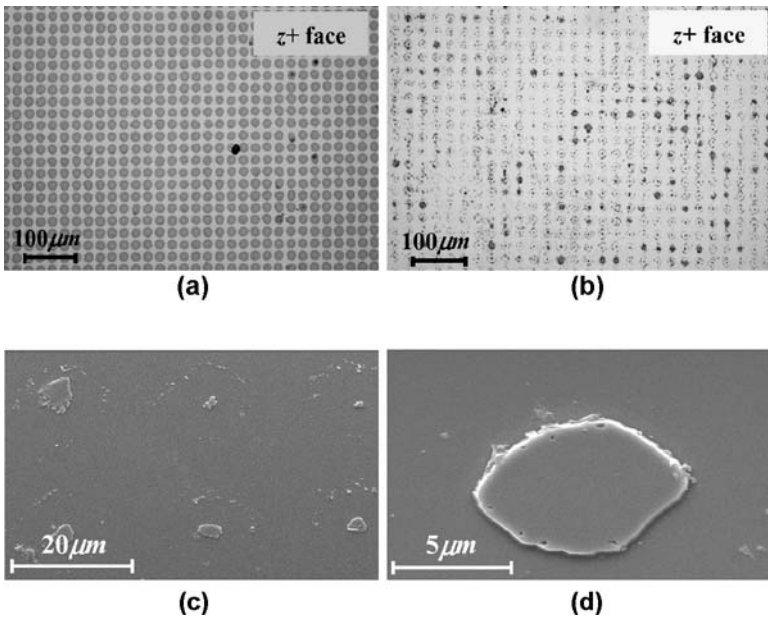


Fig. 3.16. (a) Optical microscope image of the square array of resist dots; (b) optical microscope image of the corresponding dot-like domains after wet etching; (c), (d) two different SEM magnified views of the dot-like domains. The period is around 23 μm along both X and Y crystal axis direction

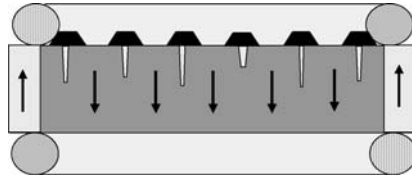


Fig. 3.17. Schematic cross section view of the un-reversed domains (*white regions*) formed under the resist dots after EFO of two-dimensional HL patterned LN samples

image in Fig. 3.16(c) shows that each dot-like domain is surrounded by smaller dot structures similar in nature to those obtained in case of one-dimensional resist pattern (see Fig. 3.13(a)) and forming a circle-like structure. The etching process reveals that the surrounding dots have the same polarization direction as the central ones. This means that the domain spreading under the resist dots evolves leaving such smaller dot-like regions un-reversed. In other words, the central dots correspond to the regions not reached at all by the domain spreading, whereas the surrounding ones result from non-homogeneous advancing of the domain wall towards the central part of the resist dots. The diameter of the circle-like structures is everywhere shorter than that of the printed resist dots by about $2\text{ }\mu\text{m}$. This means that they originate under the resist dots but not in correspondence of their edges. A quantitative characterization of these surrounding dots is carried out by comparing the mean value of the ratio p/d estimated for the resist array (Fig. 3.16(a)) and for the etched domain structure (Fig. 3.16(b)), p being the pitch of the periodic structure and d the diameter of the resist dots and of the circle-like structures, respectively. The measurements give 1.6 in case of the resist array and 1.9 in the other. This confirms the geometrical non correspondence between the surrounding dots and the resist edges. Moreover, the $Z-$ face of the sample in Fig. 3.16(b) is perfectly flat, meaning that any structure is revealed by the etching process and thus a surface reversed domain structure has been obtained. Therefore the EFO clearly evolves from the $Z-$ to the $Z+$ face leaving shallow dot-like un-reversed domains under the resist dots, as shown by the schematic cross section view in Fig. 3.17.

3.5.3 Overpoling Applied to Two-Beams Resist Gratings at Sub-Micron Scale

The application of the EFO process to samples resist patterned by the TB interferometer allowed the fabrication of periodic surface structures at sub-micron scale with different geometries [25, 34]. Four samples with different kinds of topography and periods were investigated. The samples A and B have 2D periodic structure consisting of a square array of pillar-like structures (PLS) and hole-like structures (HLS), respectively, with $2\text{ }\mu\text{m}$ period; the sample C has a 2D periodic structure consisting of a square array of HLS with 530 nm period; the sample D has a 1D periodic structure with 600 nm period. All of these samples are first domain reversed by EFO and then etched in HF solution at room temperature for 5 minutes. The PLS or the HLS are obtained by applying the EFO to samples resist patterned with a

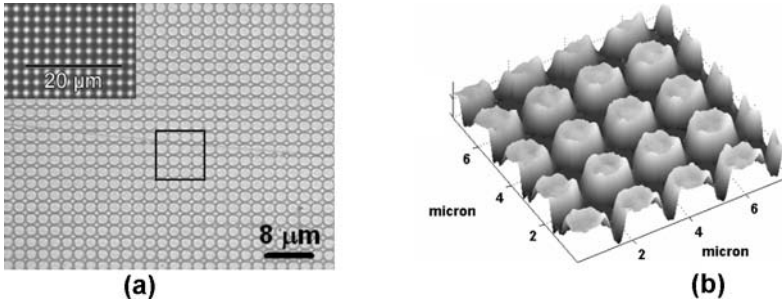


Fig. 3.18. (a) Optical microscope image of sample A and (b) corresponding surface representation of the region in the square frame. The *inset* shows the optical microscope image of the corresponding photoresist grid-like geometry

grid-like geometry (GLG) or a dot-like geometry (DLG), respectively. In fact, the EFO allows to reverse the ferroelectric polarization everywhere in the bulk crystal apart from shallow un-reversed regions under the photoresist layer which faithfully reproduce the resist pattern geometry. Figure 3.18(a) shows the optical microscope image of the Z– face of sample A, after etching, and that of the corresponding GLG resist pattern as example (see the inset).

The PLS, surrounded by canyon-like structures, obtained in sample A is clearly visible in the surface representation image in Fig. 3.18(b), corresponding to the region highlighted by the square frame in Fig. 3.18(a). The AFM topography image taken on the Z– face of the sample B is presented in Fig. 3.19(a). The HLS obtained in sample B is clearly visible in the surface view shown in Fig. 3.19(b).

The etch depth profile is around 220 nm as shown by the AFM profile measurement in Fig. 3.19(c). Figure 3.20(a) shows the AFM topography image taken on Z– face of sample C which has been overpoled by using the DLG resist pattern shown in the inset as example. A magnified view of the structure is presented in Fig. 3.20(b) while the surface view is shown in Fig. 3.20(c). The etch depth is around 1 μm as shown by the AFM profile measurement in Fig. 3.20(d). Figure 3.21(a), (b) show the AFM topography image and the corresponding profile measurement taken on the Z– face of sample D. The etch depth is around 200 nm.

Table 3.1 summarizes the main measurement results.

3.5.4 Complex Surface Structures by Moiré HL

Moiré effect [35] was used in the HL process by the TB set-up to fabricate periodic resist gratings with complex geometries to be transferred into 500 μm thick LN substrates as surface structures by EFO and subsequent wet etching. In particular, three kinds of structures are produced corresponding to three different beating geometries.

Sample M1 is resist coated on Z– face and HL patterned with 2 μm period 2D square grating by 90° crossed exposures. Afterwards, Z+ face is coated and HL

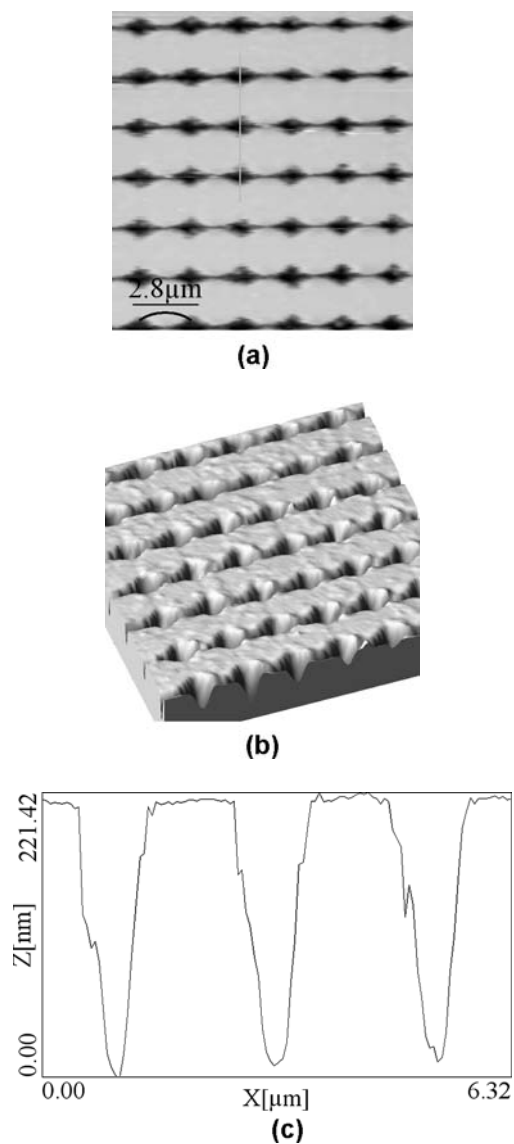


Fig. 3.19. (a) AFM topography image of sample B; (b) corresponding 3D representation; (c) depth profile along the line indicated in (a)

patterned by the same 2D pattern. Figure 3.22(a) shows the typical square array resist grating obtained on the $Z+$ face, after patterning $Z-$ face. The fringe period is slightly changed before exposing $Z+$ face, resulting in a typical moiré fringe pattern obtained on the $Z-$ face (see Fig. 3.22(c)). In fact, since the $Z-$ face is

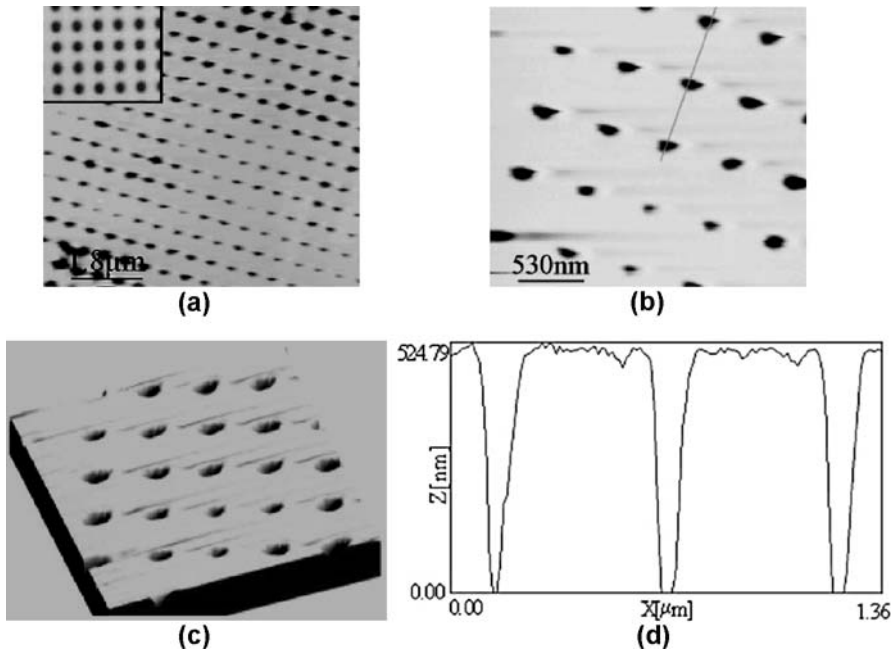


Fig. 3.20. (a) AFM topography image of sample C; (b) magnified topography view; (c) corresponding 3D image; (d) depth profile along the line indicated in (b). The *inset* shows the optical microscope image of the corresponding dot-like geometry resist pattern

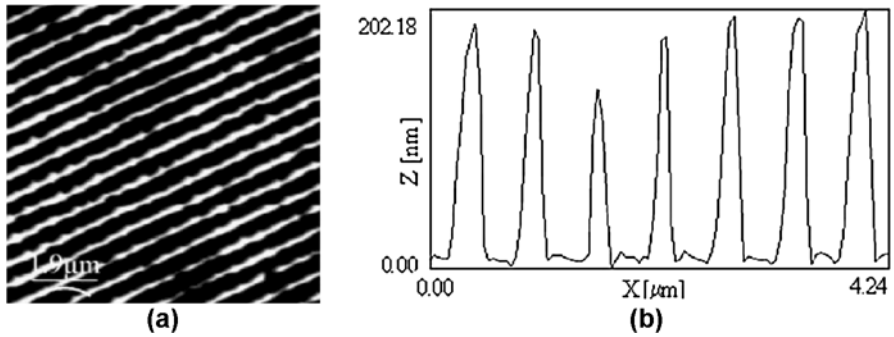


Fig. 3.21. (a) AFM topography image of sample D; (b) corresponding depth profile along a line perpendicular to the domain direction

patterned first, that effect is due to the residual resist photosensitivity on the Z− face, during the exposure of Z+.

The interference fringes, transmitted by the resist on Z+ face and by the crystal itself, overlap with the resist pattern previously printed on the Z− face, causing the well known moiré effect [35]. If necessary, this effect can be easily avoided by

Table 3.1. List of the main measurements obtained for each sample. In case of PLS the etch depth refers to the surrounding canyon-like structures

	Structure type	Period (nm)	Feature size (nm)	Etch depth (nm)	Area (mm × mm)
Sample A	PLS	2000	1500	1000	(4 × 4)
Sample B	HLS	2000	900	220	(2 × 2)
Sample C	HLS	530	200	530	(2 × 2)
Sample D	lines	600	300	200	(1 × 1)

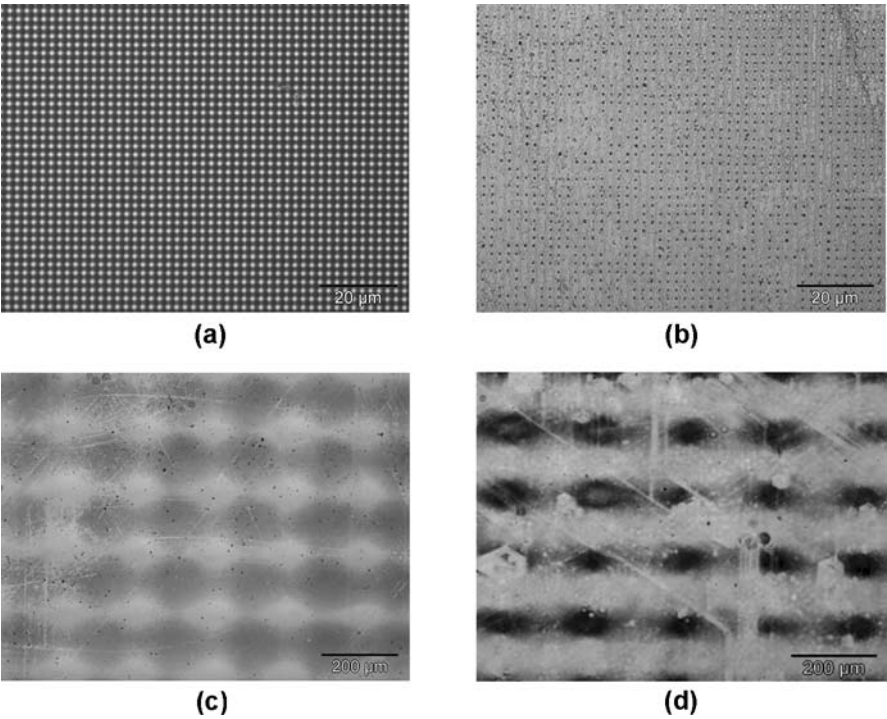


Fig. 3.22. Optical microscope image of (a) the resist grating printed on the Z+ face of sample M1; (b) the corresponding surface structure on Z+ after poling and etching; (c) the resist grating printed on the Z- face; (d) the corresponding surface structure on Z-

post-baking the sample after developing the Z- face and before spin-coating the Z+ face.

The moiré effect produces on Z- face a double period resist grating with periods 2 μm and 200 μm (see Fig. 3.22(c)). The sample is then subject to EFO and Fig. 3.22(b)–(d) show the reversed domain pattern revealed by HF etching on Z+ and Z- face, respectively. Referring to the wide field image in Fig. 3.22(d) a magnified optical microscope image is acquired in a dark region (see Fig. 3.23(a), and a SEM image is taken in one of the bright regions (see Fig. 3.23(b)). The SEM

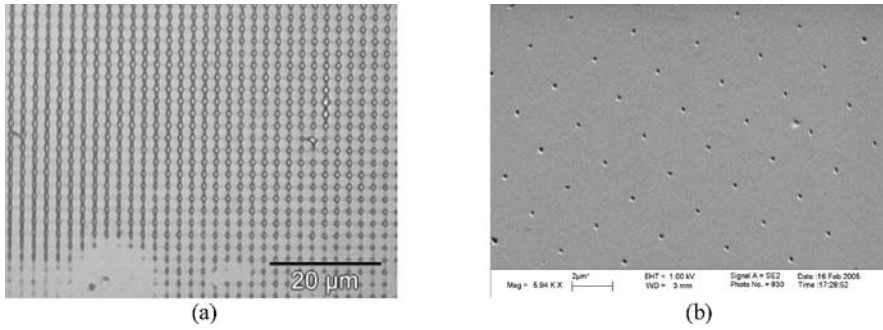


Fig. 3.23. (a) Magnified optical microscope image of sample M1 in correspondence of the regions appearing dark in wide field optical microscope image; (b) SEM image of the bright regions

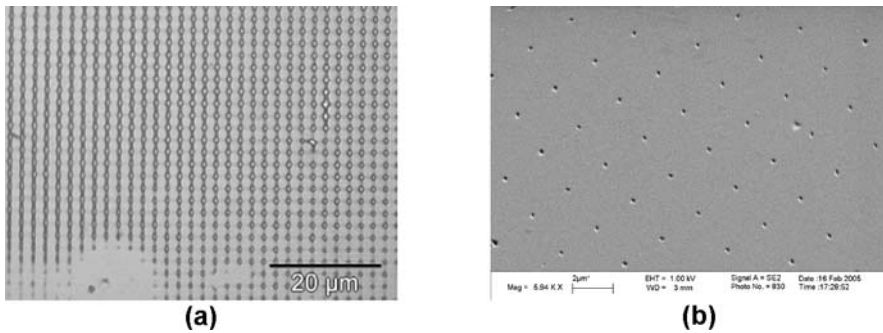


Fig. 3.24. Optical microscope image of (a) the resist grating printed on the Z- of sample M2; (b) the corresponding surface structure

image clearly shows that periodic hole-like structures around 200 nm sized have been obtained.

Sample M2 is resist coated on Z- face and subject to four HL exposures: two 90° crossed exposures at 2.4 μm period and two 90° crossed exposures at 2.5 μm period. A unique development process is performed after the four exposures. A 2D double period (2.4 μm and 2.5 μm) resist grating is obtained on Z- face as result of the moiré beating between the two fringe gratings, as shown by the optical microscope image in Fig. 3.24(a). Subsequent EFO and HF etching allows to transfer such resist geometry into the LN substrate as surface structure shown by the optical microscope image in Fig. 3.24(b).

Sample M3 is resist coated on Z- face and subject to three HL exposures: two crossed exposures at 2.4 μm period and one at 2.4 μm period. A unique development process is performed here too, after the four exposures. A 2D grating at 2.4 μm with 1D channels at 2.5 μm period is obtained as shown by the optical microscope image in Fig. 3.25(a). The surface structure obtained on Z- face by EFO and subsequent

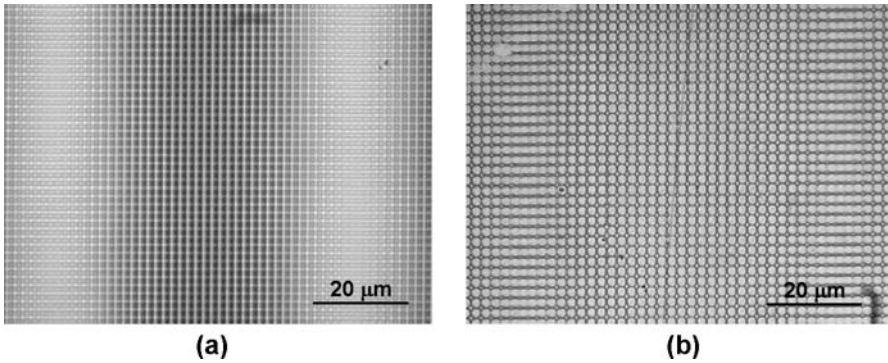


Fig. 3.25. Optical microscope image of (a) the resist grating printed on the Z– face of sample M3 and (b) the corresponding surface structure

Table 3.2. Main features of resist gratings and corresponding surface domain structures for the three kinds of samples fabricated here

	Sample M1	Sample M2	Sample M3
Moiré process	(Z+) 2D at 2 μm	(Z–) dual 2D	(Z–) 2D at 2.4 μm
	(Z–) 2D at ~2 μm	(2.4 μm; 2.5 μm)	(Z–) 1D at 2.5 μm
Resist grating	(Z+) 2D at 2 μm	(Z–) dual 2D	(Z–) 2D at 2.4 μm +
	(Z–) dual 2D (2 μm; 200 μm)	(2.4 μm; 2.5 μm)	1D at 2.5 μm (channels period 80 μm)
Domain structure	(Z+) 2D pillar at 2 μm	(Z–) dual 2D holes	(Z–) 2D holes at 2.4 μm +
	(Z–) dual 2D holes (2 μm; 200 μm)	(2.4 μm; 2.5 μm)	1D PPLN at 2.5 μm (channels period 80 μm)

HF etching is shown by the optical microscope image in Fig. 3.25(b). The 1D channels are periodic with 80 μm period.

The moiré beating geometries and the corresponding structures fabricated here are listed in Table 3.2. It is important to note that, in every case, the domain pattern obtained by the EFO process on Z– face faithfully reproduces the resist geometry.

3.6 Double-Face Sub-Micron Surface Structures

This section presents a technique for achieving double-face one-dimensional and two-dimensional sub-micron periodic surface structures over areas of about $(5 \times 5) \text{ mm}^2$ [36]. The period of the structures is 2 μm. The Z– face was resist patterned and subject to post-bake to remove the residual photosensitivity and after that the Z+ face was resist patterned. The EFO was performed as in case of the previously described samples. Different domain pattern geometries were fabricated on Z+ and Z– crystal faces to show the reliability of the technique. Sample M1 in the previous section is an example of double-face patterned sample where the

bake process at 200°C of $Z-$ face has not been performed, thus allowing the moiré effect on $Z-$ face by using the residual resist photosensitivity. In this section three different kinds of double-face patterned samples are shown: D1, D2 and D3.

Sample D1 was patterned with one-dimensional resist grating on both faces. Figure 3.26(a), (b) show the optical microscope images of the $Z-$ and $Z+$ face of the sample D1, respectively, after EFO and etching. It is worth noting that several samples have been processed like sample D1 and the 1D surface structure generated on $Z-$ face always faithfully reproduces the resist grating in each sample. In contrast, the surface structure fabricated on $Z+$ face, even though patterned with the same quality resist grating as $Z-$, exhibits a corrupted geometry (see Fig. 3.26(b)). This demonstrates that the patterning of $Z-$ face provides better quality domain gratings.

Sample D2 was patterned with a two-dimensional array of resist dots on both faces. Figure 3.27(a), (b) show the optical microscope images of the $Z-$ and $Z+$ faces of sample D2, respectively, after EFO and etching. The EFO and etching applied to the array of resist dots clearly gives an array of pillars on $Z+$ face and an array of holes on $Z-$ face. Figure 3.26(c) shows the optical microscope image of the polished and etched Y face of sample D1. This picture clearly shows that the EFO applied to double-face resist patterned samples generates surface un-reversed domains on both faces.

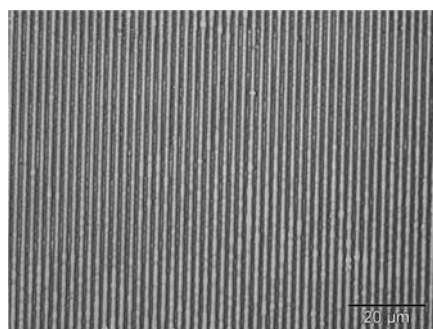
Sample D3 was fabricated with completely different domain pattern geometries on the two faces. The $Z-$ face was patterned with a two-dimensional array of resist dots and $Z+$ face was patterned with a one-dimensional resist grating. Figure 3.28(a), (b) show the optical microscope images of the $Z-$ and $Z+$ face of sample D3, respectively, after EFO and etching.

The inspection of the polished and etched Y face of these three samples reveals that the EFO generates un-reversed regions under the resist coated areas on both faces, with average depths around 10 μm , largely compatible with waveguide fabrication. Figure 3.29 shows the optical diffraction pattern of the etched sample D3, taken with a He-Ne laser aligned nearly perpendicularly to the $Z+$ face.

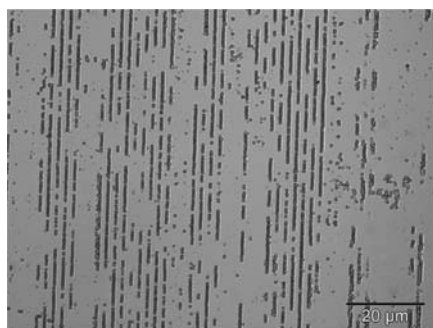
The resultant diffraction pattern represents the reciprocal lattice of the periodically poled pattern and gives information about the quality of the realized grating. In fact, by scanning the laser beam over the whole structure area of about $(5 \times 5) \text{ mm}^2$, the diffraction orders are clear and exhibit constant diffraction angles, thus demonstrating the uniformity of the structures over the whole engineered region. Moreover, the measurement of the diffraction angles is in good agreement with the space periodicity, measured by standard optical microscope.

3.7 Possible Applications for Novel Photonic Crystal Devices

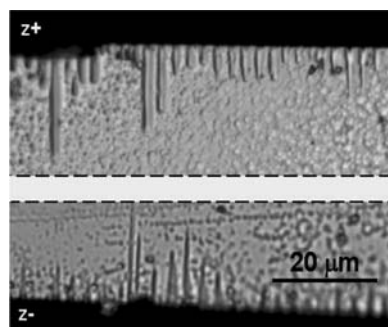
This section is aimed at proposing the LN structures described in this chapter for possible applications in the field of photonic devices. In fact, such structures exhibit specific features which allow to foresee the possibility to fabricate innovative



(a)



(b)



(c)

Fig. 3.26. Optical microscope image of (a) the etched Z− face of sample D1; (b) the corresponding etched Z+ face; (c) the corresponding polished and etched Y face

photonic devices exploiting the specific properties of the LN material (EO, PZ, non-linearity, etc.). Further investigations are currently under consideration in order to demonstrate the actual feasibility of such photonic devices.

The one-dimensional sub-micron period surface reversed domain gratings (see Fig. 3.21) could be used for different purposes in etched as well as un-etched

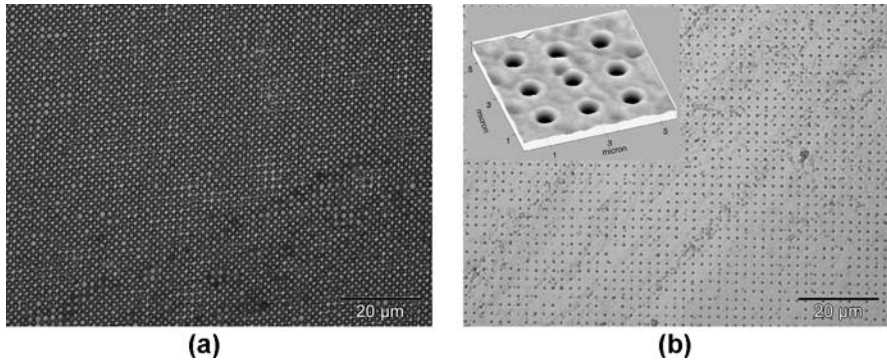


Fig. 3.27. Optical microscope image of (a) the etched Z- face of sample D2 and (b) the corresponding etched Z+ face. The *inset* shows a magnified surface view of the sample D2

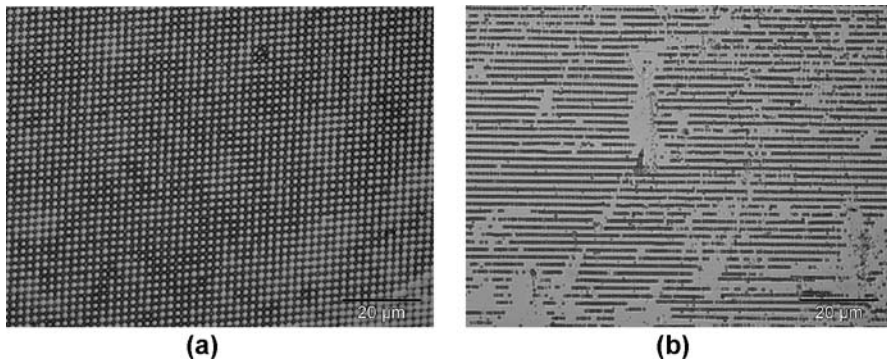


Fig. 3.28. Optical microscope image of (a) the etched Z- face of sample D3 and (b) the corresponding etched Z+ face

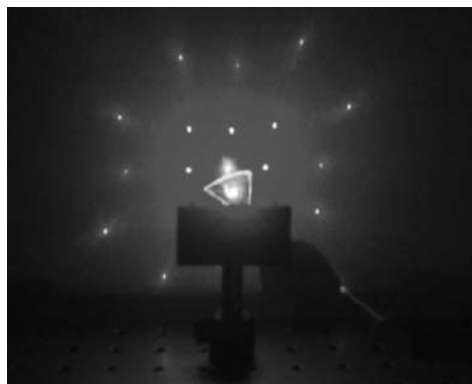


Fig. 3.29. Optical diffraction pattern of the sample D3

version. In the last case the domain grating could be implemented in waveguide configuration for the fabrication of novel nonlinear devices providing short-wavelength conversions by QPM interaction. Moreover periods down to 300 nm would allow backward nonlinear wavelength interactions. The sub-micron period of these gratings allows to foresee also their implementation in the fabrication of different innovative Bragg reflectors, depending on the etched or un-etched nature of the structure, operating in the infrared wavelength region with subsequent interesting applications in the field of telecommunications. In case of un-etched gratings a tunable Bragg reflector device would be possible by exploiting the refractive index step induced electro-optically by appropriate electrodes. In case of etched gratings a different tunable Bragg reflector would be possible by using the refractive index step between air and LN where the tunability could be induced by the EO effect as before or for example by thermal expansion with further applications in the field of sensors.

The two-dimensional short period surface domain gratings after etching could be implemented in planar waveguides for the fabrication of innovative tunable photonic band-gap devices exploiting the refractive index contrast between air and LN and the unique properties of LN (nonlinearity; electro-optics; piezoelectricity; pyroelectricity; etc.).

The moiré method allows to introduce artificial defects in a host photonic band-gap structure, thus providing the possibility to manipulate photons by localizing the electromagnetic states and “trap the light” [37]. For example, photons can propagate through a linear defect within a two-dimensional pattern. This phenomenon may be used in ultra-small optical devices for optical communications.

An interesting advantage of the double-face patterning relies on the possibility to shrink into the same chip size a number of devices twice as many and with completely different geometries on the two faces according to the requirements.

References

1. A.M. Prokhorov, Yu.S. Kuz'minov, *Physics and Chemistry of Crystalline Lithium Niobate* (Adam Hilger, Bristol, 1990)
2. L.E. Myers, R.C. Eckardt, M.M. Fejer, R.L. Byer, W.R. Bosenberg, J.W. Pierce, *J. Opt. Soc. Am. B* **12**, 2102 (1995)
3. A.A. Oliver (ed.), *Acoustic Surface Waves*. Topics in Applied Physics, vol. 24 (Springer, Berlin, 1978)
4. B.U. Chen, E. Marom, A. Lee, *Appl. Phys. Lett.* **31**, 263 (1977)
5. H.L. Garvin, E. Garmire, S. Somekh, H. Stoll, A. Yariv, *Appl. Opt.* **12**, 455 (1973)
6. B.L. Soporì, C.M. Phillips, W.S.C. Chang, *Appl. Opt.* **19**, 790 (1980)
7. C.L. Lee, C.L. Lu, *Appl. Phys. Lett.* **35**, 756 (1979)
8. K. Nassau, H.J. Levinstein, G.M. Loiacono, *Appl. Phys. Lett.* **6**, 228 (1965)
9. N. Niizeki, T. Yamada, H. Toyoda, *Jpn. J. Appl. Phys.* **6**, 318 (1967)
10. J. Webjörn, F. Laurell, G. Arvidsson, *J. Light. Technol.* **7**, 1597 (1989)
11. J.L. Jackel, R.E. Howard, E.L. Hu, S.P. Lyman, *Appl. Phys. Lett.* **38**, 907 (1981)
12. C. Ren, J. Yang, Y. Zheng, L. Chen, G. Chen, S. Tsou, *Nucl. Instrum. Methods Phys. Res. B* **19**, 1018 (1987)

13. C.I.H. Ashby, P.J. Brannon, Appl. Phys. Lett. **49**, 475 (1986)
14. K. Christensen, M. Müllenborn, Appl. Phys. Lett. **66**, 2772 (1995)
15. F. Laurell, J. Webjörn, G. Arvidsson, J. Holmberg, J. Light. Technol. **10**, 1606 (1992)
16. T.-J. Wang, C.-F. Huang, W.-S. Wang, P.-K. Wei, J. Light. Technol. **22**, 1764 (2004)
17. T.-L. Ting, L.-Y. Chen, W.-S. Wang, Photonics Technol. Lett. **18**, 568 (2006)
18. I.E. Barry, G.W. Ross, P.G.R. Smith, R.W. Eason, G. Cook, Mater. Lett. **37**, 246 (1998)
19. C. Restoin, S. Massy, C. Darraud-Taupiac, A. Barthelemy, Opt. Mater. **22**, 193 (2003)
20. J.G. Scott, A.J. Boyland, S. Mailis, C. Grivas, O. Wagner, S. Lagoutte, R.W. Eason, Appl. Surf. Sci. **230**, 138 (2004)
21. D.M. Gill, D. Jacobson, C.A. White, C.D.W. Jones, Y. Shi, W.J. Minford, A. Harris, J. Light. Technol. **22**, 887 (2004)
22. F. Lacour, N. Courjal, M.-P. Bernal, A. Sabac, C. Bainier, M. Spajer, Opt. Mater. **27**, 1421 (2005)
23. H. Hu, A.P. Milenin, R.B. Wehrspohn, H. Hermann, W. Sohler, J. Vac. Sci. Technol. A **24**, 1012 (2006)
24. H. Hu, R. Ricken, W. Sohler, R.B. Wehrspohn, Photonics Technol. Lett. **19**, 417 (2007)
25. S. Grilli, P. Ferraro, P. De Natale, B. Tiribilli, M. Vassalli, Appl. Phys. Lett. **87**, 233106 (2005)
26. J.L. Jackel, C.E. Rice, J.J. Veselka, Appl. Phys. Lett. **41**, 607 (1982)
27. J.M.M.M. de Almeida, Opt. Eng. **46**, 064601 (2007)
28. M. Yamada, N. Nada, M. Saitoh, K. Watanabe, Appl. Phys. Lett. **62**, 435 (1993)
29. V. Bermúdez, L. Huang, D. Hui, S. Field, E. Diéguez, Appl. Phys. A **70**, 591 (2000)
30. V. Pruneri, J. Webjörn, P.St.J. Russell, J.R.M. Barr, D.C. Hanna, Opt. Commun. **116**, 159 (1995)
31. V. Gopalan, Q.X. Jia, T.E. Mitchell, Appl. Phys. Lett. **75**, 2482 (1999)
32. J.P. Spallas, A.M. Hawryluk, D.R. Kania, J. Vac. Sci. Technol. B **13**, 1973 (1995)
33. M.L. Schattenburg, R.J. Aucoin, R.C. Fleming, J. Vac. Sci. Technol. B **13**, 3007 (1995)
34. P. Ferraro, S. Grilli, Appl. Phys. Lett. **89**, 133111 (2006)
35. O. Kafri, A. Livuat, Opt. Lett. **4**, 314 (1979)
36. S. Grilli, P. Ferraro, L. Sansone, M. Paturzo, S. De Nicola, G. Pierattini, P. De Natale, Photonics Technol. Lett. **18**, 541 (2006)
37. J.D. Joannopoulos, P.R. Villeneuve, S. Fan, Nature **386**, 143 (1997)

Ferroelectric Crystals for Photonic Applications
Including Nanoscale Fabrication and Characterization
Techniques

Ferraro, P.; Grilli, S.; De Natale, P. (Eds.)

2009, XVIII, 424 p., Hardcover

ISBN: 978-3-540-77963-6